Nuclear excitation functions of proton-induced reactions (E_p = 35–90 MeV) from Fe, Cu, and Al

Stephen A. Graves [a,*], Paul A. Ellison [a], Todd E. Barnhart [a], Hector F. Valdovinos [a], Eva R. Birnbaum [b], Francois M. Nortier [b], Robert J. Nickles [a], Jonathan W. Engle [b,*]

[a] University of Wisconsin – Madison, 1111 Highland Ave., Madison, WI 53705, USA
[b] Los Alamos National Laboratory, P.O. Box 1663, Los Alamos, NM 87544, USA

ARTICLE INFO

ABSTRACT

Fe, Cu, and Al stacked foils were irradiated by 90 MeV protons at the Los Alamos Neutron Science Center's Isotope Production Facility to measure nuclear cross sections for the production of medically relevant isotopes, such as ^{52g}Mn, ^{54}Mn, ^{48}Cr, ^{55}Co, ^{58m}Co and ^{57}Ni. The decay of radioactive isotopes produced during irradiation was monitored using high-purity germanium gamma spectroscopy over the months following irradiation. Proton fluence was determined using the ^{nat}Al(p,x)^{22}Na, ^{nat}Cu(p,x)^{62}Zn ^{nat}Cu(p,x)^{65}Zn, and ^{nat}Cu(p,x)^{56}Co monitor reactions. Calculated cross sections were compared against literature values and theoretical TALYS predictions. Notably this work includes the first reported independent cross section measurements of ^{nat}Cu(p,x)^{58m}Co and ^{nat}Cu(p,x)^{58g}Co.

1. Introduction

Radioisotopes of medical interest which can be produced using intermediate-energy proton accelerators (30 < E_p < 200 MeV) include the parent nuclides in generator systems ^{82}Sr/^{82}Rb, ^{68}Ge/^{68}Ga, ^{44}Ti/^{44}Sc, ^{72}Se/^{72}As, as well as direct production of ^{225}Ac. Both the Los Alamos Neutron Science Center's (LANSCE's) Isotope Production Facility (IPF) and the Brookhaven National Lab's (BNL's) Brookhaven Linac Isotope Producer (BLIP) are well suited to producing these isotopes. The national clinical supply for ^{82}Sr/^{82}Rb and ^{68}Ge/^{68}Ga generators is currently shared between these facilities by employing alternating six month run-cycles. Research tracers and generator radionuclides are produced intermittently depending on demand and the needs of the isotope program. The large-scale production of these isotopes is necessarily preceded by accurate nuclear excitation function measurements at appropriate energies.

Recently ^{52}Mn ($t_{1/2}$ = 5.59 d, β^+ = 29.6%, $E\beta_{ave}$ = 0.24 MeV) and ^{55}Co ($t_{1/2}$ = 17.5 h, β^+ = 76%, $E\beta_{ave}$ = 0.57 MeV) have been investigated preclinically as positron emission tomography (PET) imaging tracers due to their favorable physical, chemical, and biological properties [1–5]. Mn^{2+} has been shown to behave biologically like Ca^{2+}, making it an excellent candidate for applications such as neural tract tracing and pancreatic β-cell mass determination [6,7]. For intravenous injections of $^{52g}Mn^{2+}$, a blood clearance of under 5 min suggests that $^{51}Mn^{2+}$ ($t_{1/2}$ = 46.2 m, β^+ = 97.1%, $E\beta_{ave}$ = 0.962 MeV) could be a clinically desirable surrogate for ^{52g}Mn from a dosimetry and pharmacokinetic perspective [6,7]. Both ^{52}Mn and ^{55}Co have well established chelation chemistries, and are rapidly and stably coordinated by DOTA at a neutral pH. With established chelation methods, both ^{52}Mn and ^{55}Co may be employed in a variety of molecular imaging applications, such as *in vivo* tracking of monoclonal antibodies [1]. Mn^{2+} is also a versatile T1-shortening magnetic resonance imaging (MRI) contrast agent, which could enable future dual modality PET/MR applications [8,9]. In addition

* Corresponding authors at: 1005 WIMR, 1111 Highland Ave., Madison, WI 53705, USA (S.A. Graves). P.O. Box 1663, Los Alamos, NM, 57545, USA (J.W. Engle).
E-mail addresses: sagraves@wisc.edu (S.A. Graves), jwengle@lanl.gov (J.W. Engle).
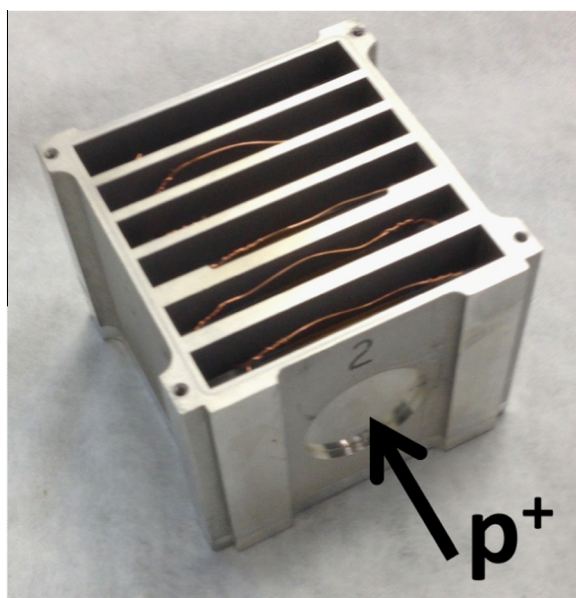
to ^{52g}Mn and ^{55}Co, ^{58m}Co has been suggested to have decay properties suitable for Auger electron therapeutic applications, and to this end several preclinical studies are underway [10–12].

The radioactive half-lives of ^{55}Co and ^{52}Mn are conducive to national and international transport, respectively. Some issues which need to be addressed prior to considering large-scale production of these isotopes include preclinical demand, target design considerations, radionuclide yield, radionuclidic purity, and methods for radiochemical isolation. The goal of this work was to measure the nuclear formation cross sections of ^{52}Mn, ^{54}Mn, ^{55}Co, and others from ^{nat}Fe and ^{nat}Cu foils in an attempt to address expected radionuclide yield and purity. Furthermore, we employ multiple monitor reactions to correct for beam energy inaccuracies derived from proton transport simulations and calculations.

2. Materials and methods

2.1. Target-stack design and irradiation

A target stack was constructed using 50 μm and 25 μm ^{nat}Fe foils (99.99%, GoodFellow Metals, Coraopolis, PA, 15108–9302, USA), 100 μm and 30 μm ^{nat}Cu foils (99.9%, GoodFellow Metals), and 100 μm ^{nat}Al foils (99.997%, Alfa Aesar, Ward Hill, MA, 01835, USA). Foils were cut into 2.5 cm squares and weight measurements were taken. Degrader foil widths and heights were each measured with a Vernier caliper in three places. Target foil thicknesses (atoms/cm^2) were calculated from width, height, and weight measurements. Foils were then sealed in 25 μm Kapton® polyimide tape with a silicone-based adhesive backing. The resulting encapsulated target foils were affixed to frames and placed within a water-proof target stack box, containing degrader layers, shown in Fig. 1. Degrader densities were calculated by dimensional measurements and weighing, prior to being affixed to the target box by electron beam welding. Each target stack compartment contained two ^{nat}Fe foils, one ^{nat}Cu foil, and one ^{nat}Al foil. At the front and rear of the target stack, 130 μm thick stainless steel layers were employed as beam profile monitors. Details of this target stack design are listed in Table 1.

The assembled target stack was irradiated at the Los Alamos National Laboratory (LANL) Isotope Production Facility (IPF) with approximately 99 nA of incident protons for one hour. Nominal proton energy was 100 MeV, but time-of-flight measurements during the irradiation indicated an average incident proton energy of 99.7 MeV. This measured incident energy was used for further calculations and simulations. After passing through an entrance window, a layer of cooling water, and the target window, the average beam energy was approximately 90 MeV. Following irradiation, the target-stack was disassembled, and the encapsulated foils were wiped clean of surface contamination. Foils were monitored for gamma emissions beginning approximately 24 h following irradiation.

2.2. Gamma spectroscopy

Following irradiation, gamma spectroscopy was performed using two high-purity germanium (HPGe) detectors at LANL (p-type Al-window ORTEC GEM detectors) and one detector at the University of Wisconsin – Madison (UW) (Canberra C1519). Early post-irradiation assays were done at LANL, and later assays were done at UW-Madison. In the case of LANL data, spectral peak areas were determined using the SPECANAL code, which is an in-house revised version of the legacy GAMANAL code [13]. In the case of UW data, spectral peak areas were determined using the SAMPO code, which employs particularly sophisticated peak-fitting methods [14]. Decay-corrected comparisons between UW and LANL quantification agreed within 5%. Uncertainty in activity

Table 1
Target stack order and foil thicknesses, where the proton beam travels through the stack in the order shown in the table. Uncertainty in aerial density is calculated from uncertainties in the width, height, and mass of individual foils. Degrader thickness measurements are omitted due to the proton transport methods used herein.

Target layer	Nominal thickness	Measured thickness (atoms/cm^2)	Thickness uncertainty (%)
SS profile monitor	130 μm	–	–
Fe-1	50 μm	3.56E+20	0.09%
Al-1	100 μm	5.88E+20	0.33%
Cu-1	100 μm	9.26E+20	0.18%
Fe-2	50 μm	3.88E+20	0.17%
Al Degrader-1	4.983 mm	–	–
Fe-3	50 μm	3.48E+20	0.18%
Al-2	100 μm	5.94E+20	0.05%
Cu-2	30 μm	2.23E+20	0.87%
Fe-4	50 μm	3.78E+20	0.19%
Al Degrader-2	4.394 mm	–	–
Fe-5	50 μm	3.41E+20	0.05%
Al-3	100 μm	5.94E+20	0.11%
Cu-3	30 μm	2.24E+20	0.41%
Fe-6	50 μm	3.80E+20	0.14%
Al Degrader-3	3.468 mm	–	–
Fe-7	25 μm	1.87E+20	0.25%
Al-4	100 μm	5.93E+20	0.12%
Cu-4	30 μm	2.27E+20	1.24%
Fe-8	25 μm	1.77E+20	0.55%
Al Degrader-4	3.460 mm	–	–
Fe-9	25 μm	1.86E+20	0.44%
Al-5	100 μm	5.90E+20	0.14%
Cu-5	30 μm	2.21E+20	0.98%
Fe-10	25 μm	1.69E+20	0.21%
Al Degrader-5	3.465 mm	–	–
Fe-11	25 μm	1.78E+20	0.17%
Al-6	100 μm	5.92E+20	0.14%
Cu-6	30 μm	2.23E+20	1.27%
Fe-12	25 μm	1.84E+20	0.48%
SS Profile Monitor	130 μm	–	–

Fig. 1. Photograph of target stack before being sealed with o-ring bearing lid. Beam entrance window is shown, as are Al degrader layers between stack compartments. Degrader layers were measured and weighed before being electron-beam welded into place. Target frame bundles are held together by copper wire, as shown.

quantification was calculated as the quadrature sum of (1) the statistical counting uncertainty, (2) uncertainty in literature branching ratio data, and (3) uncertainty in the HPGe efficiency calibrations.

2.3. Initial beam energy determination

Average beam energy for each target position was estimated using the Monte Carlo N-Particle (MCNP6) code and by in-house calculations using Anderson & Ziegler (A&Z) analytic formalisms [15,16]. A&Z calculations provide reasonable estimations of average beam energy, but MCNP6 simulations yield both average energy and the energy distribution at each target position [17]. A plot of proton energy distribution full-width half-max (FWHM) vs. average proton energy from MCNP6 results, shown in Fig. 2, was used for further FWHM calculations.

2.4. Monitor reactions

Four monitor reactions were selected in an attempt to provide accurate measures of proton fluence with minimal neutron contamination: $^{nat}Cu(p,x)^{56}Co$, $^{nat}Cu(p,x)^{62}Zn$, $^{nat}Cu(p,x)^{65}Zn$, and $^{nat}Al(p,x)^{22}Na$. These reactions have been extensively characterized, and are recommended by the IAEA as proton monitor reactions [18]. For fluence calculations, recommended IAEA cross sections values were used. In-house evaluated data were used above 60 MeV for the $^{nat}Cu(p,x)^{62}Zn$ reaction. Proton fluence uncertainty was calculated as the quadrature sum of (1) the uncertainty in recommended monitor reaction cross sections, (2) monitor reaction isotope quantification uncertainty, (3) uncertainty in the target foil aerial density, and (4) the uncertainty in the "effective cross section" from the proton energy distribution FWHM at each monitor foil. Note that uncertainty (1) and (4) both have an energy dependence which must be accounted for in subsequent calculations.

2.5. Final energy determination: multiple monitor reaction variance minimization

Making the assumptions that monitor reaction-derived proton fluence should agree across multiple monitor reactions within the same target stack compartment and that the proton energy distribution FWHM values predicted by MCNP6 simulations are accurate, then it is possible to use multiple monitor reactions to determine the average proton energy at each monitor foil. This approach has the potential to greatly reduce proton energy uncertainties toward the rear of a target stack. Monitor reaction-derived fluence discrepancies have previously been described [17], pointing to uncertainties in degrader thickness, degrader density, incident beam energy, and proton stopping power data.

In this work, agreement in the proton fluences derived from the four monitor reactions on ^{nat}Cu and ^{nat}Al foils in the final stack compartment was obtained by minimizing variance in the calculated fluence as a function of Al degrader density in analytic A&Z proton transport calculations. Varying degrader density has little effect on average beam energy near the front of the stack, but changes the average proton energy greatly toward the rear of the stack. This minimization method, shown in Fig. 3, is a straightforward and effective way of estimating average beam energy. An average proton energy of 35.1 MeV entering the last compartment was found, approximately 8 MeV lower than MCNP6 simulations and approximately 6 MeV lower than A&Z calculations with a nominal Al density. The impact of this variance minimization process on monitor reaction-derived proton fluence is shown in Fig. 4. Although only degrader density was varied in this approach, it is likely that the source of this energy discrepancy is a combination of uncertainty in incident beam energy, literature stopping powers, target geometry, and degrader density.

2.6. Fluence loss characterization

As the beam travels through the stack, small angle deflections cause a broadening in the beam profile. Using the activated stainless steel profile monitors from the front and rear of the target stack, Gafchromic™ film was exposed and analyzed yielding beam profile measurements. These profile measurements were used to determine a theoretical fluence loss based on the finite target foil areas. This theoretical fluence loss agreed within error compared with monitor reaction derived fluence loss, as shown in Fig. 5.
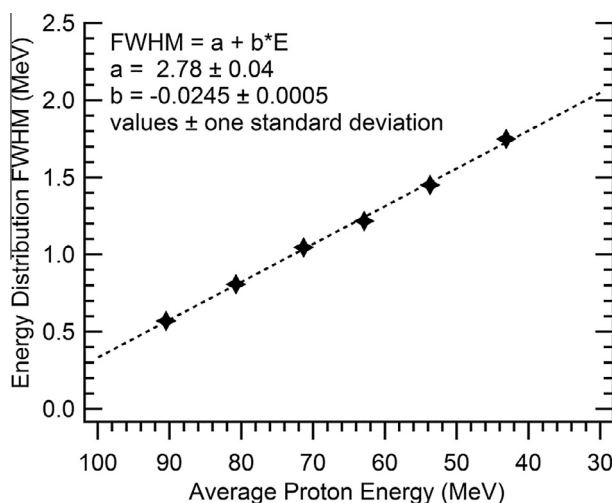

Fig. 2. MCNP6 simulation results showing energy distribution full-width half-max (FWHM) as a function of average proton energy in each target stack compartment. A linear least-squares fit was used for determining proton energy FWHM at non-simulated energies.
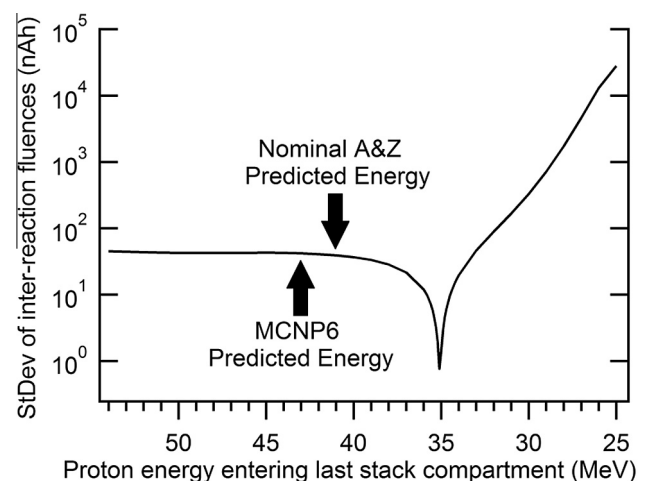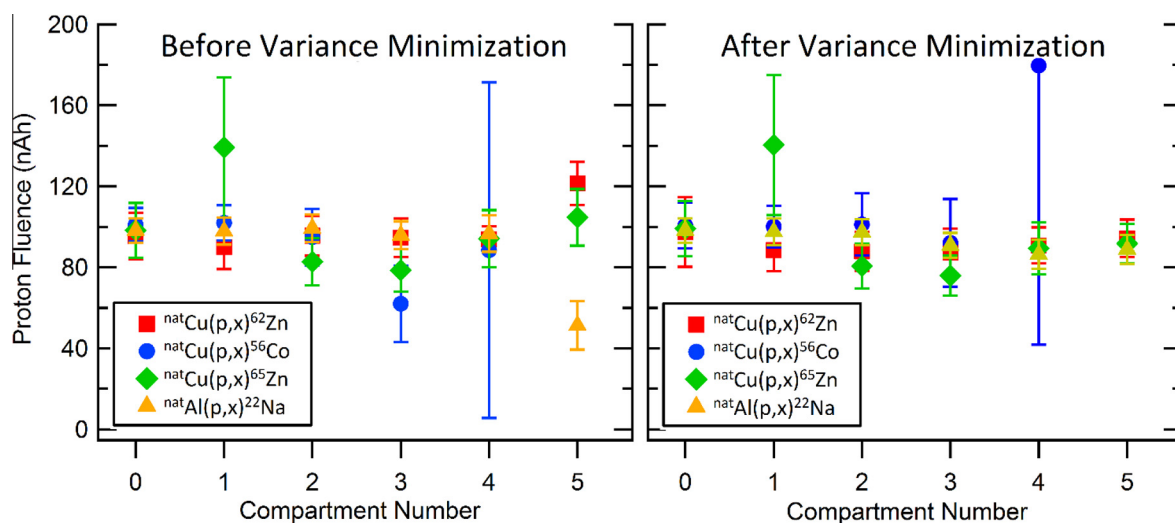

Fig. 3. Results of varying degrader density in analytic A&Z calculations on inter-monitor reaction fluence standard deviation. Varying degrader density has the effect of non-linearly varying the average beam energy in each compartment. This non-linear dependence on density has nearly the same functional impact as variations in the incident beam energy. Arrows indicate the predicted average beam energy in the last stack compartment by MCNP6 simulation and nominal A&Z calculations. A clear minimum from this approach is seen at 35.1 MeV, suggesting the initial beam energy estimations by nominal A&Z calculations and by MCNP6 simulation are significantly higher than what was experimentally observed.

Fig. 4. Results of varying degrader density in analytic A&Z calculations on inter-monitor reaction fluence variance. Compartment #0 resides at the front of the target stack, while compartment #5 resides at the rear. A significant reduction in monitor reaction variance throughout the entire stack is seen after employing the variance minimization approach in compartment #5. This result is further evidence that multiple monitor reaction variance minimization has the potential to significantly reduce energy uncertainties in stacked-foil cross section measurement experiments. The variability of $^{nat}Cu(p,x)^{56}Co$ in compartment 4 and absence in compartment 5 is due to the rapid drop off in this excitation function at these energies.
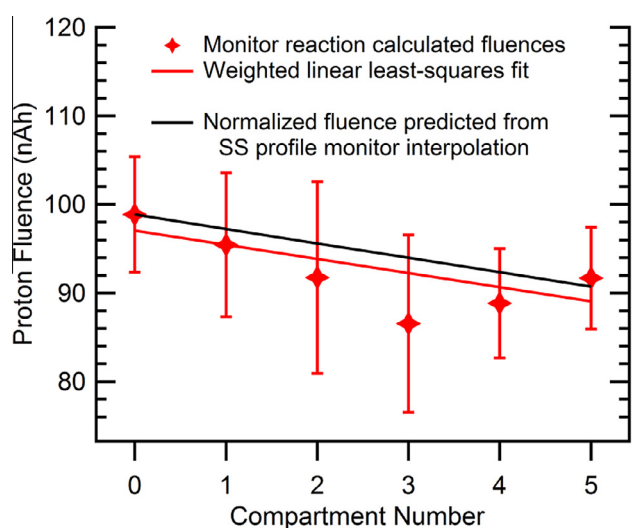
Fig. 5. Final fluence measurements as a function of target stack compartment number following monitor reaction derived proton fluence variance minimization. The red line represents a weighted linear line of regression indicating a drop in proton fluence of 7.2% as the beam travelled through the target stack. The black line is the estimated fluence loss determined by analysis of the stainless steel (SS) beam profile foils at the front and rear of the stack, normalized to the proton fluence measured in the first compartment.

2.7. Cross section calculations

Where possible, activation products were quantified at multiple time-points. End of bombardment (EoB) activities and uncertainties were determined by extrapolation of decay curve regression, weighted by quantification uncertainty for individual time-points. Radioactive half-lives and gamma branching ratios were obtained from the Brookhaven National Laboratory National Nuclear Data Center (NNDC). For posterity, these values are listed in Appendix A. For indirectly produced daughter isotopes, EoB activity quantification was achieved by least-squares fitting with solutions to the first and second-order Bateman differential equations. One example of this relationship is the $^{nat}Fe(p,x)^{48}Cr$

reaction, where ^{48}Cr ($t_{1/2}$ = 21.56 h) subsequently decays to ^{48}V ($t_{1/2}$ = 15.97 d). Cross sections were calculated as the EoB activity (s^{-1}) divided by the aerial target density (cm^{-2}), proton fluence (unitless), and the radioactive decay constant (s^{-1}). For purposes of analysis, cumulative cross sections (σ_c) were defined as the sum of all independent formation cross sections (σ_i) leading to that particular radionuclide. This distinction is relevant in cases of decay chains or the formation of metastable states.

3. Results and discussion

The target-stack box remained water-tight during irradiation, and foils were not thermally deformed. The layer of Kapton® tape surrounding each foil bubbled slightly on the front and rear of each foil near the beam spot. From irradiated Al foils, ^{22}Na was the only isotope quantified. From irradiated Cu foils ^{55}Co, ^{57}Co, ^{58}Co, ^{60}Co, ^{61}Cu, ^{64}Cu, ^{59}Fe, ^{52}Mn, ^{54}Mn, ^{56}Ni, and ^{57}Ni were quantified, but ^{59}Fe was excluded from cross section calculation due to insufficient counting statistics (Table 2). From Fe foils, ^{55}Co, ^{56}Co, ^{57}Co, ^{58}Co, ^{48}Cr, ^{51}Cr, ^{52}Fe, ^{52}Mn, ^{54}Mn, and ^{48}V were quantified, but ^{57}Co and ^{58}Co were excluded from cross section calculation due to limited counting statistics and concerns over background contamination (Table 3). The nuclear cross sections measured in this work are compared to literature values in Appendix B. From the four monitor reactions used herein, proton fluence entering the target stack was measured to be 98.9 ± 6.5 nAh. This is in excellent agreement with the 99 nAh nominal fluence from IPF operation logs, which is based on non-destructive proton current measurement. By the final target stack compartment, measured proton fluence had dropped by approximately 7.2–91.7 ± 5.8 nAh.

Uncertainty in calculated cross sections was typically driven by uncertainty in proton fluence derived from monitor reactions (±6–12%) and HPGe calibration uncertainty (±~5%). In a few particular cases, uncertainty was driven by activity quantification uncertainty due to limited counting statistics. Target foils had thickness uncertainties less than 1.3%, indicating that foil characterization uncertainty did not contribute significantly to overall cross section uncertainty.

The prospect of producing positron emitting isotopes of nickel is intriguing from the perspective of essential trace-element

Table 2
Measured cross sections for ^{nat}Cu+p reaction products. σ_c denotes cumulative cross section values, while σ_i denotes independent cross sections.

^{nat}Cu+p E$_p$ (MeV)	^{55}Co σ$_c$ (mb)	^{57}Co σ$_c$ (mb)	^{58g}Co σ$_c$ (mb)	^{58g}Co σ$_i$ (mb)	^{58m}Co σ$_i$ (mb)	^{60}Co σ$_c$ (mb)	^{61}Cu σ$_c$ (mb)	^{64}Cu σ$_c$ (mb)	^{52g}Mn σ$_c$ (mb)	^{54}Mn σ$_c$ (mb)	^{56}Ni σ$_c$ (mb)	^{57}Ni σ$_c$ (mb)
89.4 ± 0.6	1.60 ± 0.11	36.8 ± 2.4	51.7 ± 3.4	20.8 ± 5.2	30.9 ± 5.6	10.2 ± 0.8	58.9 ± 4.7	37.4 ± 2.8	1.45 ± 0.01	6.36 ± 0.40	0.0824 ± 0.0056	1.31 ± 0.09
78.6 ± 0.9	0.788 ± 0.069	31.2 ± 2.7	45.7 ± 3.9	18.8 ± 6.5	27.2 ± 6.8	10.1 ± 0.9	65.6 ± 5.8	40.5 ± 4.0	0.376 ± 0.035	3.93 ± 0.37	0.0878 ± 0.0077	0.985 ± 0.086
69.1 ± 1.1	0.108 ± 0.014	34.3 ± 4.1	36.4 ± 4.3	12.4 ± 6.1	24.2 ± 6.7	10.2 ± 1.2	78.4 ± 7.6	41.3 ± 5.3	–	4.76 ± 0.52	0.0762 ± 0.0091	1.35 ± 0.16
58.6 ± 1.4	–	49.6 ± 5.8	30.3 ± 3.6	6.0 ± 5.8	24.4 ± 6.5	11.3 ± 1.3	85.4 ± 9.1	48.2 ± 6.1	–	4.92 ± 0.53	0.0169 ± 0.0025	2.09 ± 0.25
48.0 ± 1.6	–	36.6 ± 2.6	42.8 ± 3.1	18 ± 11	25.3 ± 11.2	8.59 ± 0.74	118 ± 13	52.9 ± 5.4	–	0.907 ± 0.095	–	0.981 ± 0.075
35.1 ± 1.9	–	40.0 ± 4.3	44.5 ± 2.9	7.4 ± 10.3	36.9 ± 10.6	3.72 ± 0.29	168 ± 23	68.7 ± 6.4	–	0.066 ± 0.012	–	–

Table 3
Measured cross sections for ^{nat}Fe+p reaction products. σ_c denotes cumulative cross section values, while σ_i denotes independent cross sections.

^{nat}Fe+p E$_p$ (MeV)	^{55}Co σ$_c$ (mb)	^{56}Co σ$_c$ (mb)	^{48}Cr σ$_c$ (mb)	^{51}Cr σ$_c$ (mb)	^{52}Fe σ$_c$ (mb)	^{52g}Mn σ$_c$ (mb)	^{54}Mn σ$_c$ (mb)	^{48}V σ$_c$ (mb)
90.2 ± 0.6	4.77 ± 0.32	6.21 ± 0.58	0.749 ± 0.050	78.1 ± 5.1	2.42 ± 0.16	35.3 ± 2.3	73.7 ± 4.9	15.8 ± 1.0
89.0 ± 0.6	4.48 ± 0.30	6.49 ± 0.59	0.666 ± 0.044	74.0 ± 4.9	2.36 ± 0.16	36.7 ± 2.4	75.1 ± 5.0	14.8 ± 1.0
79.3 ± 0.8	5.40 ± 0.46	8.07 ± 0.89	0.398 ± 0.034	61.9 ± 5.3	2.55 ± 0.22	39.3 ± 3.4	78.3 ± 6.7	7.20 ± 0.62
78.3 ± 0.9	5.39 ± 0.46	7.68 ± 0.82	0.392 ± 0.034	61.0 ± 5.2	2.64 ± 0.23	43.1 ± 3.7	82.9 ± 7.1	7.03 ± 0.60
68.8 ± 1.1	6.52 ± 0.77	8.37 ± 1.12	0.372 ± 0.044	48.6 ± 5.8	2.28 ± 0.27	37.1 ± 4.4	88.0 ± 10.4	5.16 ± 0.61
67.8 ± 1.1	6.48 ± 0.77	9.32 ± 1.26	0.371 ± 0.044	50.7 ± 6.0	2.21 ± 0.26	38.5 ± 4.6	94.3 ± 11.2	5.50 ± 0.65
59.3 ± 1.3	8.09 ± 0.94	13.2 ± 1.8	0.304 ± 0.035	63.9 ± 7.4	1.67 ± 0.19	21.0 ± 2.4	110 ± 13	6.77 ± 0.79
58.3 ± 1.4	8.07 ± 0.94	12.5 ± 1.8	0.263 ± 0.031	65.0 ± 7.6	1.57 ± 0.18	19.6 ± 2.3	113 ± 13	6.87 ± 0.80
48.8 ± 1.6	10.1 ± 0.7	14.4 ± 1.4	0.0406 ± 0.0046	97.2 ± 6.8	1.64 ± 0.12	13.9 ± 1.0	148 ± 10	5.34 ± 0.38
47.6 ± 1.6	10.1 ± 0.7	14.5 ± 1.5	0.0136 ± 0.0045	95.1 ± 6.7	1.62 ± 0.11	14.6 ± 1.0	152 ± 11	4.82 ± 0.35
36.1 ± 1.9	18.3 ± 1.2	20.9 ± 2.0	–	48.0 ± 3.0	1.31 ± 0.08	26.9 ± 1.7	147 ± 9	0.139 ± 0.024
34.6 ± 1.6	22.3 ± 1.4	18.8 ± 1.7	–	36.3 ± 2.3	2.10 ± 0.14	31.4 ± 2.0	136 ± 9	–

biological research or as a possible theranostic pair with ^{66}Ni ($t_{1/2}$ = 54.6 h, β^- = 100%, Eβ^-_{ave} = 73.4 keV), which decays by soft β^- emission that could bridge the gap between Auger emitting nuclides and conventional therapeutic β-emitting isotopes. The production cross section for ^{56}Ni by ^{nat}Cu(p,x)^{56}Ni is insufficient for medical relevance at energies below 100 MeV (max of 0.085 mb), but production cross section for ^{57}Ni ($t_{1/2}$ = 35.6 h, β^+ = 43.6%, Eβ^+_{ave} = 354 keV) is more reasonable with a peak of approximately 2.2 mb at 57 MeV.

Production of cobalt isotopes from ^{nat}Cu+p could be useful as experimental monitor reactions (^{nat}Cu(p,x)^{56}Co in particular), but otherwise there are relatively few potential applications for this production route. One notable feature of this work however is the first reported independent cross section data for ^{nat}Cu(p, x)^{58m}Co and ^{nat}Cu(p,x)^{58g}Co. The calculated cumulative cross section values from these independent measures agree well with measured cumulative data. The production of ^{58m}Co appears to be more probable than the direct production of ^{58g}Co at the energies probed here. In Fig. 6 these measured independent and cumulative cross are compared against TALYS/TENDL-2015 code predictions [19]. The code agrees with measured independent ^{nat}Cu(p,x)^{58g}Co cross sections, but seems to underestimate ^{nat}Cu (p,x)^{58m}Co cross sections. This underestimation is also reflected in the cumulative ^{nat}Cu(p,x)^{58g}Co TALYS predictions.

Production of ^{52g}Mn by ^{nat}Cu+p appears impractical due to the large co-production of ^{54}Mn (approximately 4:1 atomic ratio, ^{54}Mn:^{52g}Mn at 90 MeV) and because the cross section is significantly lower than ^{nat}Fe(p,x)^{52g}Mn at intermediate energies (30–100 MeV) or ^{nat}Cr(p,x)^{52g}Mn at low energies (10–20 MeV). Producing ^{52g}Mn at intermediate energies by ^{nat}Fe(p,x) is possibly viable, depending on the required radionuclidic purity. The instantaneous production rates for ^{52g}Mn, ^{54}Mn, ^{48}Cr, and ^{51}Cr as a function of energy are shown in Fig. 7. These results suggest that a ^{nat}Fe target that degrades a proton beam from 90 to 70 MeV would initially yield approximately 47 MBq/μAh of ^{52}Mn with an overall post-separation radionuclidic purity of 96.5%. With low energy production approaches (i.e. ^{nat}Cr(p,x)^{52g}Mn) being capable of
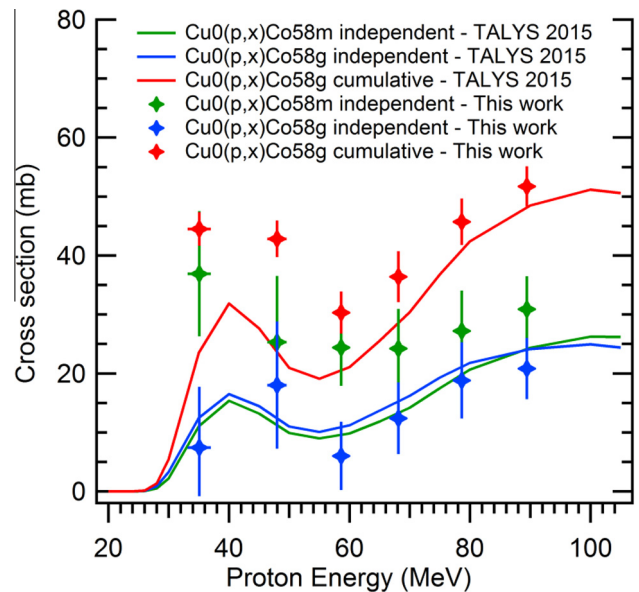
Fig. 6. Comparison between TALYS 2015 predictions and measured independent ^{nat}Cu(p,x)^{58g}Co and ^{nat}Cu(p,x)^{58m}Co and cumulative ^{nat}Cu(p,x)^{58g}Co cross sections. TALYS predicted values for the independent ^{nat}Cu(p,x)^{58g}Co agree with values measured in this work, but TALYS appears to underestimate ^{nat}Cu(p,x)^{58g}Co reaction cross sections. This underestimation is also reflected in the cumulative ^{nat}Cu(p, x)^{58g}Co TALYS predicted values.

radionuclidic purities greater than 99.6% [20], this production route does not appear practical. An enriched ^{54}Fe target could possibly be employed to prevent ^{54}Mn co-production. Unfortunately, the dominant reaction from this route to the A = 52 isobar, ^{54}Fe (p,3n)^{52}Co, leads entirely to ^{52m}Mn rather than ^{52g}Mn through ^{52}Co → ^{52g}Fe → ^{52m}Mn [21]. There is a need for ^{54}Fe(p,x)^{52g}Mn thick target yield experiments to evaluate the feasibility of this
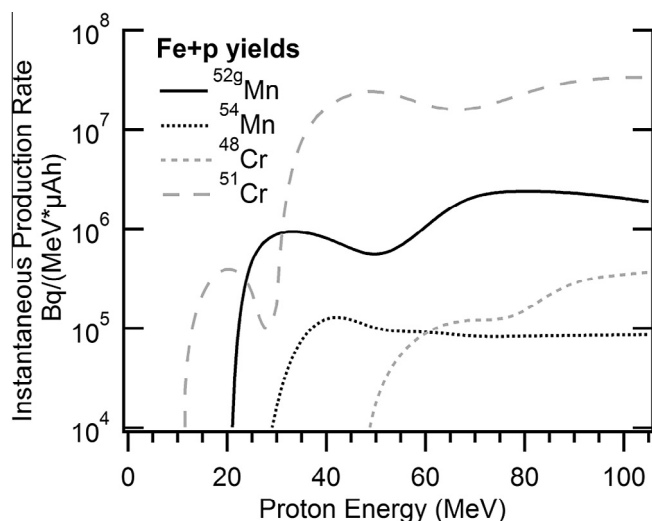
Fig. 7. Instantaneous production rate for ^{52g}Mn, ^{54}Mn, ^{48}Cr, and ^{51}Cr, including indirect production routes. Production rate is specified in units of Bq/(MeV*µAh) where MeV is the amount of beam energy lost in the target. For thin targets, production rate can be determined directly from this plot, but for thick targets an average production rate must first be calculated over the relevant energy region.

production route for radionuclidically pure ^{52g}Mn. For production schemes from Fe metal, radiomanganese could be easily isolated from radiocobalt by anion exchange chromatography, but separating Mn and Cr typically requires more elaborate radiochemistry approaches, such as ethanol-based anion exchange chromatography, trioctylamine solvent extraction, or acetic acid/methanol based anion exchange chromatography [1,9,22,23].

The use of ^{nat}Cu(p,x)^{62}Zn and ^{nat}Cu(p,x)^{65}Zn as monitor reactions has proven quite effective in this work. These reactions are already recommended by the IAEA who has evaluated literature data for this purpose. Unlike ^{nat}Al(p,x)^{22}Na and ^{nat}Cu(p,x)^{56}Co, these monitor reactions are not confounded by neutron induced reactions. As neutron flux may be significant toward the rear of a target stack, this trait should be considered when selecting monitor reactions for future studies.

4. Conclusions

From this work, we present twenty sets of cross section measurements from Fe+p and Cu+p at energies between 34.6 MeV and 90.2 MeV, including the first reported independent ^{nat}Cu(p,x)^{58g}Co and ^{nat}Cu(p,x)^{58m}Co measurements. Furthermore, we have described monitor reaction variance minimization methods which can effectively reduce proton energy uncertainties in stacked-foil cross section measurement experiments.

Acknowledgements

Appendix A

Nuclear decay data used in this work

Nuclear decay data used in this work, including radioactive half-life, prominent gamma energies, and branching ratios. Data was obtained from the National Laboratory National Nuclear Data Center (NNDC), accessed May 1st, 2016.

| Isotope	Half life	Gamma energy (keV)	Branching ratio (%)
^{22}Na	2.6018(22) y	1274.5	99.944(14)
^{24}Na	14.997(12) h	1368.6	99.9936(15)
		2754.0	99.855(5)
^{48}V	15.9735(25) d	983.5	99.98(4)
		1312.1	98.2(3)
		944.1	7.870(7)
^{48}Cr	21.56(3) h	308.3	100
		112.4	96.0(20)
^{51}Cr	27.7010(11) d	320.1	9.910(10)
^{52g}Mn	5.591(3) d	1434.1	100.0(14)
		935.5	94.5(13)
		744.2	90.0(12)
^{54}Mn	312.20(20) d	834.8	99.9760(10)
^{52g}Fe	8.275(8) h	168.7	99.2(19)
		377.7	1.643(19)
^{55}Co	17.53(3) h	931.3	75
		477.2	20.2(14)
		1408.4	16.88(8)
^{56}Co	77.27(3) d	846.8	100
		1238.3	67.6(4)
		2598.5	17.28(15)
^{57}Co	271.79(9) d	122.1	85.60(17)
		136.5	10.68(8)
		14.4	9.16(15)
^{58g}Co	70.86(7) d	810.8	99
^{60}Co	5.2714(5) y	1332.5	99.9856(4)
		1173.2	99.9736(7)
^{56}Ni	6.077(12) d	158.4	98.8(10)
		811.9	86.0(9)
		750.0	49.5(12)
^{57}Ni	35.60 h	1377.6	81.7(16)
		127.2	16.7(3)
		1919.5	12.26(25)
^{61}Cu	3.333(5) h	283.0	12.2(3)
		656.0	10.77(18)
		67.4	4.23(13)
^{64}Cu	12.700(2) h	1345.8	0.473(10)
^{62}Zn	9.186(13) h	596.6	26
		40.8	25.5(13)
		548.3	15.3(8)
^{65}Zn	244.26(26) d	1115.5	50.04(24)

Appendix B

Cross section values plotted with literature data [2,24–48]
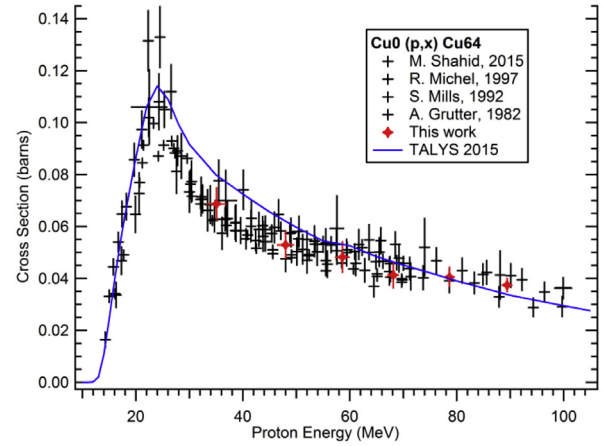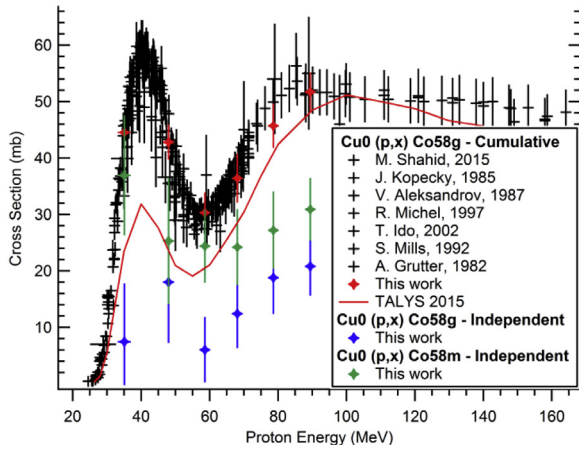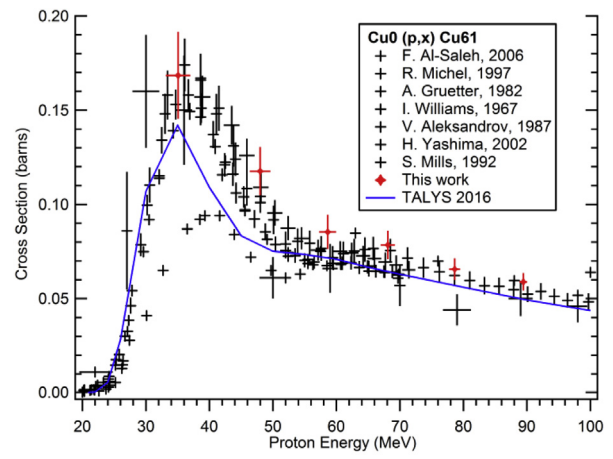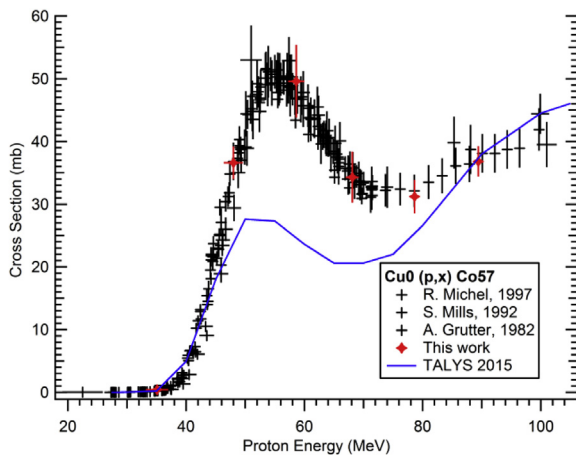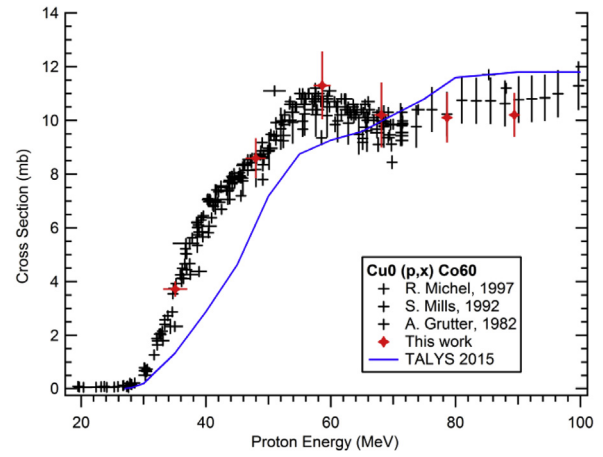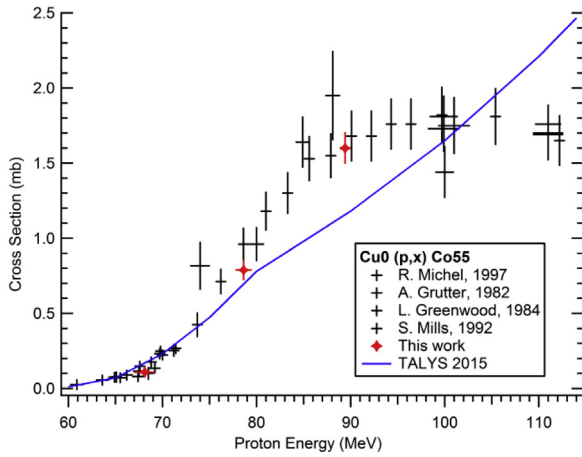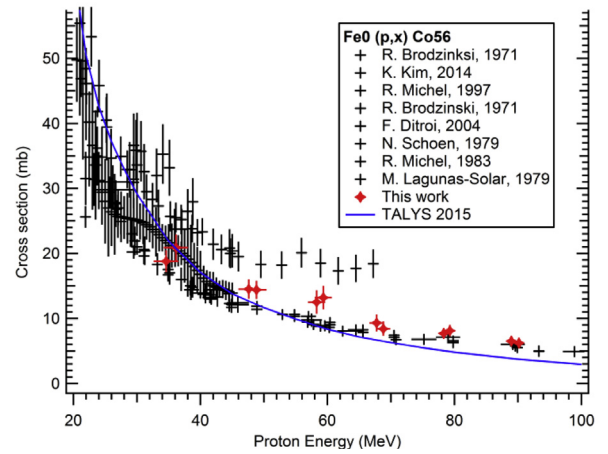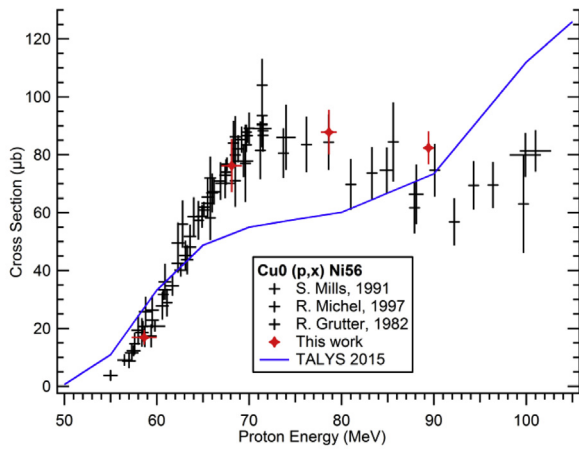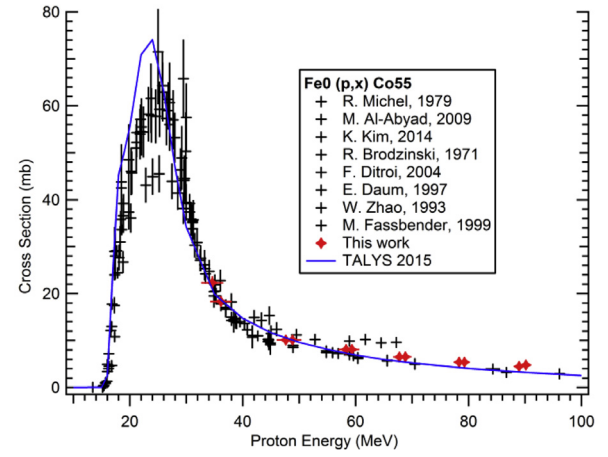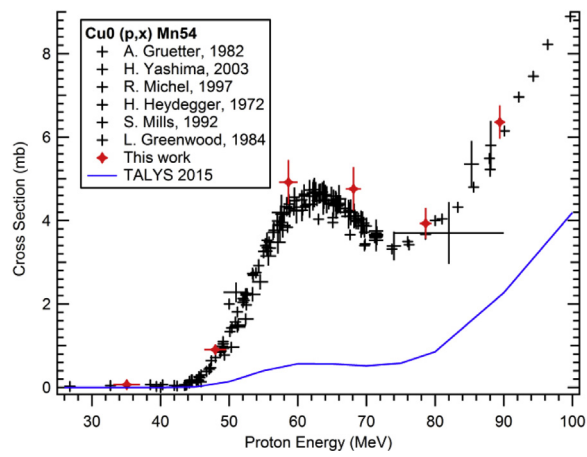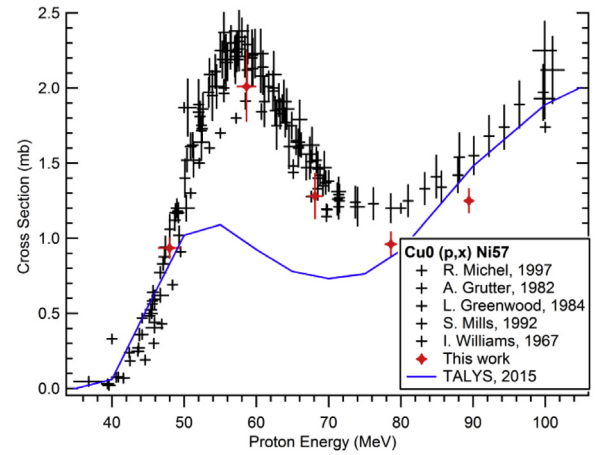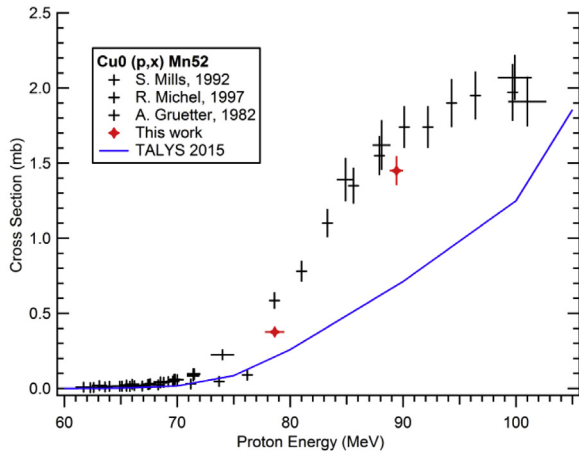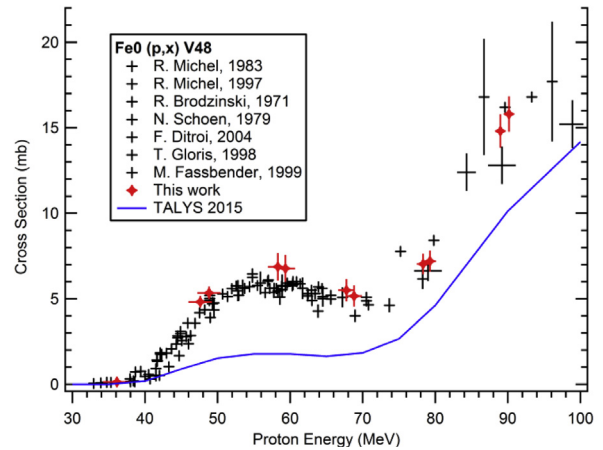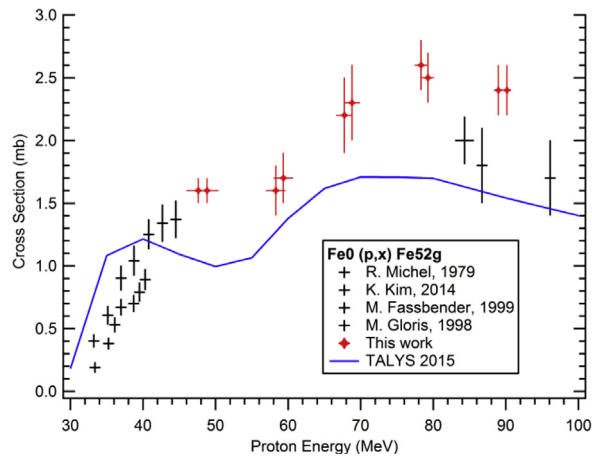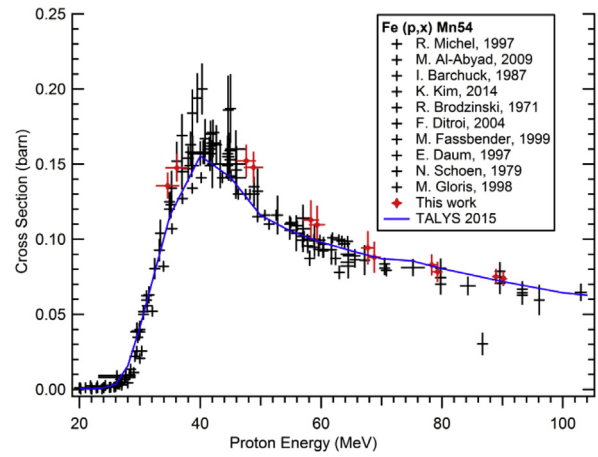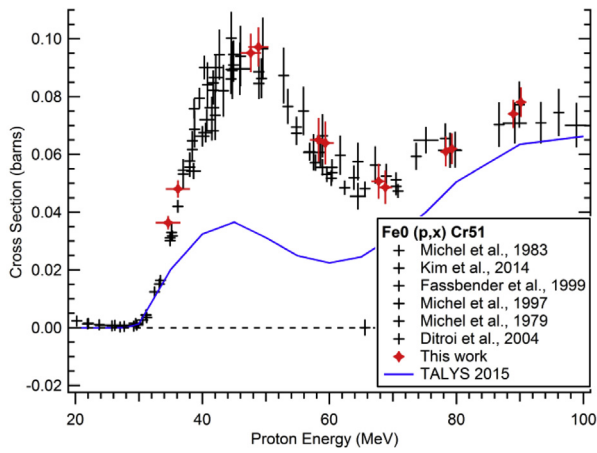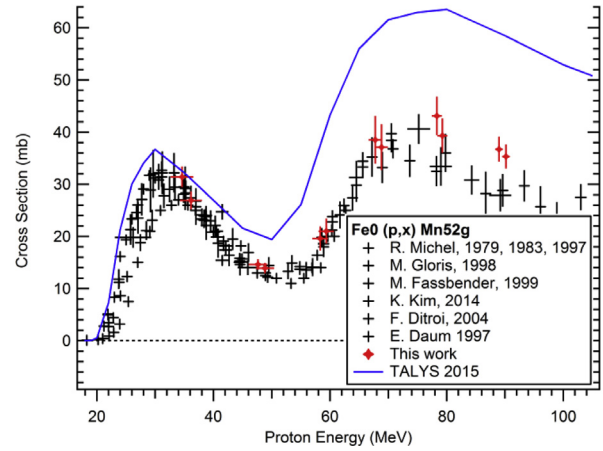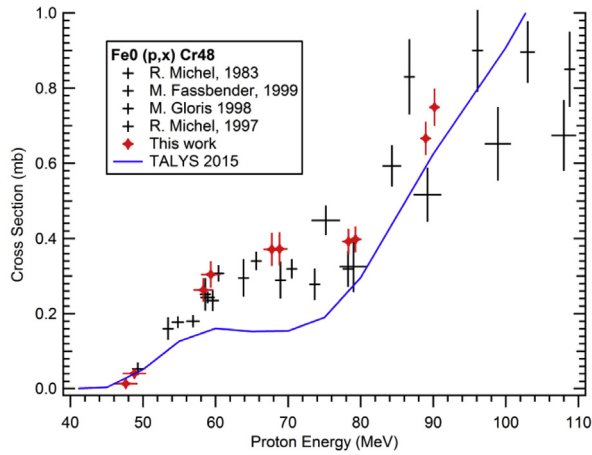
References

[1] S.A. Graves, R. Hernandez, J. Fonslet, C.G. England, H.F. Valdovinos, T.E. Barnhart, D.R. Elema, C.P. Theuer, W. Cai, Novel preparation methods of [52]Mn for ImmunoPET imaging, Bioconjug. Chem. 26 (2015) 2118–2124.

[2] M. Lagunas-Solar, J. Jungerman, Cyclotron production of carrier-free cobalt-55, a new positron-emitting label for bleomycin, Int. J. Appl. Radiat. Isotopes 30 (1979) 25–32.

[3] T. Mastren, B.V. Marquez, D.E. Sultan, E. Bollinger, P. Eisenbeis, T. Voller, S.E. Lapi, Cyclotron production of high–specific activity [55]Co and in vivo evaluation of the stability of [55]Co metal-chelate-peptide complexes, Mol. Imag. 14 (2015), 7290.2015. 00025.

[4] G.J. Topping, P. Schaffer, C. Hoehr, T.J. Ruth, V. Sossi, Manganese-52 positron emission tomography tracer characterization and initial results in phantoms and in vivo, Med. Phys. 40 (2013) 042502.

[5] H. Valdovinos, S. Graves, T. Barnhart, R. Nickles, [55]Co separation from proton irradiated metallic nickel, in: Xiii Mexican Symposium on Medical Physics vol. 1626 (2014). pp. 217–220.

[6] S. Graves, H. Valdovinos, T. Barnhart, R. Nickles, Novel [51]Mn production methods for calcium channel transport based applications, J. Nucl. Med. 57 (2016) 380.

[7] R. Hernandez, S. Graves, C. England, J. Jeffery, R. Nickles, W. Cai, Radio-manganese PET imaging of pancreatic beta cells, J. Nucl. Med. 57 (2016) 5.

[8] C.L. Brunnquell, R. Hernandez, S.A. Graves, I. Smit-Oistad, R.J. Nickles, W. Cai, M.E. Meyerand, Uptake and retention of manganese contrast agents for PET and MRI in the rodent brain, Contr. Media Mol. (2016), in press.

[9] C.M. Lewis, S.A. Graves, R. Hernandez, H.F. Valdovinos, T.E. Barnhart, W. Cai, M. E. Meyerand, R.J. Nickles, M. Suzuki, [52]Mn production for PET/MRI tracking of human stem cells expressing divalent metal transporter 1 (DMT1), Theranostics 5 (2015) 227.

[10] P. Bernhardt, E. Forssell-Aronsson, L. Jacobsson, G. Skarnemark, Low-energy electron emitters for targeted radiotherapy of small tumours, Acta Oncol. 40 (2001) 602–608.

[11] H. Valdovinos, R. Hernandez, S. Goel, S. Graves, T. Barnhart, W. Cai, R. Nickles, Cyclotron production of [58m]Co for Auger electron-based targeted radioimmunotherapy and PET imaging post-therapy with the daughter [58g]Co, J. Nucl. Med. 57 (2016) 332.

[12] H.F. Valdovinos, R. Hernandez, S. Goel, S. Graves, T. Barnhart, W. Cai, R.J. Nickles, Auger electron-based targeted radioimmunotherapy with [58m]Co, a feasibility study, in: Medical Physics: Fourteenth Mexican Symposium on Medical Physics vol. 1747 (2016). pp. 080006.

[13] R. Gmmink, J. Niday, Computerized Quantitative Analysis by Gamma-ray Spectrometry: Description of the GAMANAL Program (1972).

[14] P. Aarnio, M. Nikkinen, J. Routti, SAMPO 90 High resolution interactive gamma-spectrum analysis including automation with macros, J. Radioanal. Nucl. Chem. 160 (1992) 289–295.

[15] J.F. Ziegler, Stopping of energetic light ions in elemental matter, J. Appl. Phys. 85 (1999) 1249–1272.

[16] T. Goorley, M. James, T. Booth, F. Brown, J. Bull, L. Cox, J. Durkee, J. Elson, M. Fensin, R. Forster, Initial MCNP6 release overview, Nucl. Technol. 180 (2012) 298–315.

[17] L. Marus, J. Engle, K. John, E. Birnbaum, F. Nortier, Experimental and computational techniques for the analysis of proton beam propagation through a target stack, Nucl. Instrum. Methods Phys. Res., Sect. B 345 (2015) 48–52.

[18] F. Tárkányi, S. Takács, K. Gul, A. Hermanne, M. Mustafa, M. Nortier, P. Oblozinsky, S. Qaim, B. Scholten, Y.N. Shubin, Beam monitor reactions. Charged particle cross-section database for medical radioisotope production: Diagnostic radioisotopes and monitor reactions, IAEA-TECDOC-1211, Vienna, 2001, 49.

[19] A.J. Koning, S. Hilaire, M.C. Duijvestijn, TALYS-1.0, in: International Conference on Nuclear Data for Science and Technology 2007. pp. 211–214.

[20] A.L. Wooten, B.C. Lewis, S.E. Lapi, Cross-sections for (p, x) reactions on natural chromium for the production of 52, 52m, 54 Mn radioisotopes, Appl. Radiat. Isot. 96 (2015) 154–161.

[21] H. Junde, H. Su, M. Chunhui, Nuclear data sheets for A= 52, Nucl. Data Sheets 108 (2007) 773–882.

[22] S. Lahiri, D. Nayak, G. Korschinek, Separation of no-carrier-added [52]Mn from bulk chromium: A simulation study for accelerator mass spectrometry measurement of [53]Mn, Anal. Chem. 78 (2006) 7517–7521.

[23] M. Buchholz, I. Spahn, H.H. Coenen, Optimized separation procedure for production of no-carrier-added radiomanganese for positron emission tomography, Radiochim. Acta 103 (2015) 893–899.

[24] M. Al-Abyad, M. Comsan, S. Qaim, Excitation functions of proton-induced reactions on nat Fe and enriched [57]Fe with particular reference to the production of [57]Co, Appl. Radiat. Isot. 67 (2009) 122–128.

[25] V. Aleksandrov, M. Semyonova, V. Semyonov, Excitation functions for radionuclides produced by (p, x) reactions of copper and nickel, Atomnaya Energiya 62 (1987) 411.

[26] F. Al-Saleh, A. Al-Harbi, A. Azzam, Excitation functions of proton induced nuclear reactions on natural copper using a medium-sized cyclotron, Radiochim. Acta 94 (2006) 391–396.

[27] I. Barchuk, V. Bulkin, V. Kuz'menko, P. Kurilo, Y.N. Lobach, A. Ogorodnik, V. Prokopenko, V. Sklyarenko, V. Tokarevskii, Excitation functions of reactions caused by the interaction of protons with energies of up to 67 MeV and nuclei of silicon and iron, At. Energ. 63 (1987) 528–532.

[28] R. Brodzinski, L. Rancitelli, J. Cooper, N. Wogman, High-energy proton spallation of iron, Phys. Rev. C 4 (1971) 1257.

[29] E. Daum, Investigation of light ion induced activation cross sections in iron proton induced activation cross sections, Fed Rep Germ Rep 43 (1997).

[30] F. Ditrói, F. Tárkányi, J. Csikai, M. Uddin, M. Hagiwara, M. Baba, Investigation of Activation Cross Sections of the Proton Induced Nuclear Reactions on Natural Iron at Medium Energies, AIP Conf. Proc. 769 (2005) 1011.

[31] M. Fassbender, Y.N. Shubin, S. Qaim, Formation of Activation Products in Interactions of Medium Energy Protons with Na, Si, P, S, Cl, Ca and Fe. Radiochimica Acta 84 (1999) 59–68.

[32] M. Gloris, R. Michel, F. Sudbrock, U. Herpers, P. Malmborg, B. Holmqvist, Proton-induced production of residual radionuclides in lead at intermediate energies, Nucl. Instrum. Methods Phys. Res., Sect. A 463 (2001) 593–633.

[33] L. Greenwood, R. Smither, Measurement of Cu spallation cross sections at IPNS, 1984.

[34] A. Grütter, Excitation functions for radioactive isotopes produced by proton bombardment of Cu and Al in the energy range of 16 to 70 MeV, Nucl. Phys. A 383 (1982) 98–108.

[35] H. Heydegger, C. Garrett, A. Van Ginneken, Thin-target cross sections for some Cr, Mn, Fe Co, Ni, and Zn nuclides produced in copper by 82-to 416-MeV protons, Phys. Rev. C 6 (1972) 1235.

[36] T. Ido, A. Hermanne, F. Ditrói, Z. Szücs, I. Mahunka, F. Tárkányi, Excitation functions of proton induced nuclear reactions on [nat]Rb from 30 to 70 MeV. Implication for the production of [82]Sr and other medically important Rb and Sr radioisotopes, Nucl. Instrum. Methods Phys. Res., Sect. B 194 (2002) 369–388.

[37] K. Kim, M.U. Khandaker, H. Naik, G. Kim, Excitation functions of proton induced reactions on nat Fe in the energy region up to 45 MeV, Nucl. Instrum. Methods Phys. Res., Sect. B 322 (2014) 63–69.

[38] P. Kopecký, Proton beam monitoring via the Cu(p, x)[58]Co, [63]Cu(p, 2n)[62]Zn and [65]Cu(p, n)[65]Zn reactions in copper, Int. J. Appl. Radiat. Isotopes 36 (1985) 657–661.

[39] R. Michel, R. Bodemann, H. Busemann, R. Daunke, M. Gloris, H.-J. Lange, B. Klug, A. Krins, I. Leya, M. Lüpke, Cross sections for the production of residual nuclides by low-and medium-energy protons from the target elements C, N, O, Mg, Al, Si, Ca, Ti, V, Mn, Fe Co, Ni, Cu, Sr, Y, Zr, Nb, Ba and Au, Nucl. Instrum. Methods Phys. Res., Sect. B 129 (1997) 153–193.

[40] R. Michel, G. Brinkmann, On the depth-dependent production of radionuclides (44 ≤ A ≤ 59) by solar protons in extraterrestrial matter, J. Radioanal. Chem. 59 (1980) 467–510.

[41] R. Michel, G. Brinkmann, H. Weigel, W. Herr, Measurement and hybrid-model analysis of proton-induced reactions with V, Fe and Co, Nucl. Phys. A 322 (1979) 40–60.

[42] R. Michel, R. Stueck, F. Peiffer, Proton-Induced Reaction on Ti, V, Mn, Fe, Co, and Ni Ions, 1983.

[43] S. Mills, G. Steyn, F. Nortier, Experimental and theoretical excitation functions of radionuclides produced in proton bombardment of copper up to 200 MeV. International journal of radiation applications and instrumentation. Part A, Appl. Radiat. Isot. 43 (1992) 1019–1030.

[44] M. Shahid, K. Kim, H. Naik, M. Zaman, S.-C. Yang, G. Kim, Measurement of excitation functions in proton induced reactions on natural copper from their threshold to 43 MeV, Nucl. Instrum. Methods Phys. Res., Sect. B 342 (2015) 305–313.

[45] Z. Wenrong, L. Hanlin, Y. Weixiang, Measurement of cross sections by bombarding Fe with protons up to 19 MeV, Chin. J. Nucl. Phys. 15 (1993) 337–340.

[46] I. Williams, C. Fulmer, Excitation functions for radioactive isotopes produced by protons below 60 MeV on Al, Fe, and Cu, Phys. Rev. 162 (1967) 1055.

[47] H. Yashima, Y. Uwamino, H. Sugita, T. Nakamura, S. Ito, A. Fukumura, Projectile dependence of radioactive spallation products induced in copper by high-energy heavy ions, Phys. Rev. C 66 (2002) 044607.

[48] N. Schoen, G. Orlov, R. McDonald, Excitation functions for radioactive isotopes produced by proton bombardment of Fe Co, and W in the energy range from 10 to 60 MeV, Phys. Rev. C 20 (1979) 88.